JGR Space Physics

RESEARCH ARTICLE
10.1029/2018JA026177

New Diagnosis for Energy Flow From Solar Wind to Ionosphere During Substorm: Global MHD Simulation

Y. Ebihara[1], T. Tanaka[2], and N. Kamiyoshikawa[1,3]

[1]Research Institute for Sustainable Humanosphere, Kyoto University, Uji, Japan, [2]International Center for Space Weather Science and Education, Kyushu University, Fukuoka, Japan, [3]Now at Information Technology R&D Center, Mitsubishi Electric Corporation, Kamakura, Japan

Key Points:
- We investigated energy flow and conversion from solar wind magnetic energy and solar wind kinetic energy to ionosphere during substorm
- A large amount (~33–88%) of magnetic energy across the magnetopause originates from the solar wind kinetic energy
- Stored/released magnetic energy in the lobe and ionospheric Joule heating during expansion are regulated by solar wind parameters

Correspondence to:
Y. Ebihara,
ebihara@rish.kyoto-u.ac.jp

Citation:
Ebihara, Y., Tanaka, T., & Kamiyoshikawa, N. (2019). New diagnosis for energy flow from solar wind to ionosphere during substorm: Global MHD simulation. *Journal of Geophysical Research: Space Physics*, *124*, 360–378. https://doi.org/10.1029/2018JA026177

Received 9 OCT 2018
Accepted 7 JAN 2019
Accepted article online 10 JAN 2019
Published online 28 JAN 2019

Abstract To investigate the energy involved by a substorm, we performed global magnetohydrodynamics simulation for different solar wind conditions. The intensity of the auroral electrojet increases with the southward component of interplanetary magnetic field (IMF) and the solar wind velocity, which is consistent with observations. To evaluate the energy that enters the magnetosphere, we first defined a solar wind effective cross-sectional area in which all the Poynting fluxes entering the magnetosphere pass through. We found that the solar wind magnetic energy is insufficient to provide the magnetic energy entering the magnetosphere (intake magnetic energy) for southward IMF. About 33–88% of the intake magnetic energy is converted from the solar wind kinetic energy. About 2–7% of the solar wind kinetic energy (passing through the effective area) is converted to the magnetic energy that enters the magnetosphere. Significant contribution from the solar wind kinetic energy makes the energy coupling function complicated. The effective area also depends on the solar wind parameters, also making it complicated. An interesting point is that the rates of energy stored and released in the lobe also depend on the solar wind parameters. The ionospheric Joule heating rate is well correlated with the intake magnetic energy at onset, and during the substorm expansion. The correlation coefficients between them are better than that of the ε parameter. These results imply that both the directly driven process (manifested by intake magnetic energy) and loading-unloading process (manifested by stored/released energy in the lobe) are largely regulated by the solar wind condition.

Plain Language Summary The Sun emits energy in two different forms. One is electromagnetic waves (including visible lights), which causes tropospheric disturbances, such as tornados and hurricanes. The other one is solar wind (being composed of charged particles), which causes geomagnetic disturbances and brilliant aurora, known as magnetic storms and substorms. Previously, the magnetic energy carried by the solar wind is thought to be a major source of the geomagnetic disturbances. Using large-scale computer simulation, we found that about 33–88% of the magnetic energy entering the magnetosphere comes from the kinetic energy of the solar wind. The kinetic energy is efficiently converted to the magnetic energy just outside the magnetosphere. The amount of energy consumed in the ionosphere is found to depend on the solar wind parameters. This may imply that the magnitude of the substorm is determined by the solar wind parameters and is predictable.

1. Introduction

A large amount of energy, exceeding 10^{11} W, is consumed in the auroral ionosphere during the substorm expansion phase (Ahn et al., 1983; Kamide et al., 1986; Richmond et al., 1990; Sun et al., 1985). The ultimate source of the energy consumed in the ionosphere is the solar wind (Akasofu, 1979). The importance of the southward component of the interplanetary magnetic field (southward IMF B_z or SBZ) is noticed in 1960s (Fairfield & Cahill, 1966; Rostoker & Fälthammar, 1967). The beginning of the substorm is accompanied with either a commencement or a gradual enhancement of the magnetospheric convection (McPherron, 1970). The period from the enhancement of the magnetospheric convection to the expansion onset is called a growth phase. Perreault and Akasofu (1978) considered the Poynting flux in the interplanetary space, and an *opening* area in which the Poynting flux enters the magnetosphere. By multiplying the Poynting flux and the opening area, they obtained the following empirical equation:

$$\varepsilon(\mathrm{erg/s}) = V_{SW} {B_{IMF}}^2 {l_0}^2 \sin^4 \frac{\theta}{2}, \quad (1)$$

where $l_0 \approx 7$ Re, V_{SW} is the solar wind speed, B_{IMF} is the magnitude of IMF, and θ is the angle from the north ($\equiv \tan^{-1} B_y/B_z$). In the MKS unit, equation (1) is written as (Koskinen & Tanskanen, 2002)

$$\varepsilon(\mathrm{W}) = \frac{4\pi}{\mu_0} V_{SW} {B_{IMF}}^2 {l_0}^2 \sin^4 \frac{\theta}{2}, \quad (2)$$

where μ_0 is the magnetic constant. Akasofu (1980) suggested that a substorm expansion onset occurs when ε exceeds ~10^{11} W.

In addition to the electromagnetic energy, the kinetic energy of the solar wind may also be a source of the energy entering the magnetosphere (Nishida, 1983; Vasyliunas et al., 1982). The ratio of the kinetic energy flux to the electromagnetic energy flux through the same area is of the order of (Koskinen & Tanskanen, 2002)

$$\frac{\rho {V_{SW}}^3}{V_{SW} {B_{IMF}}^2/\mu_0} = \frac{{V_{SW}}^2}{{V_A}^2} = M_A^2, \quad (3)$$

where ρ is the mass density, V_A is the Alfvén speed, and M_A is the Alfvén Mach number. Usually, M_A is much greater than 1 in the solar wind, so that the kinetic energy flux dominates the electromagnetic energy flux. According to the dimensional analysis made by Vasyliunas et al. (1982), the net kinetic energy can be related to the ε parameter when the scale length of the magnetopause is proportional to $(\rho {V_{SW}}^2)^{-1/6}$.

As the solar wind plasma approaches the magnetosphere, the solar wind kinetic energy is first converted to the internal energy and the electromagnetic energy at the bow shock (Tanaka, 2007). After that, for SBZ, the kinetic energy is converted to the internal energy, followed by the kinetic energy and the electromagnetic energy. The last process, conversion from the kinetic energy to the electromagnetic energy, is regarded as a mantle dynamo (Siscoe et al., 2000; Tanaka, 1995, 2000). As the electromagnetic energy propagates into the lobe, the magnetic energy in the lobe increases for SBZ prior to the substorm expansion onset, and it decreases in the expansion phase (Caan et al., 1975). The release of the magnetic energy stored in the lobe is thought to be large enough to sustain the substorm (Hones, 1979). Multipoint observations have also shown that the magnetic energy stored in the lobe is sufficient to drive observed dissipation processes (Baker et al., 1997). The energy is efficiently transferred from the open field-line region (lobe) to the closed field-line region across the magnetic separatrix associated with the near-Earth reconnection (Hesse, 1995).

Baker et al. (1997) investigated energy budgets from the solar wind to the energy loss including the ring current injection, ionospheric Joule heating, auroral precipitation, auroral luminosity, auroral kilometric radiation, and plasmoids. However, the transport path of the electromagnetic energy to the ionosphere is a matter of issue. The global the global magnetohydrodynamics (MHD) simulation provides a direct way to investigate the flow and conversion of the energy. One such way is to draw an integral curve of the Poynting flux (hereinafter, referred to as an *S* curve) (Ebihara & Tanaka, 2017; Papadopoulos et al., 1999). The *S* curve originating from the solar wind penetrates the lobe region and traverses the magnetic separatrix. After traversing the separatrix, a bundle of the *S* curve split into two. One turns to dusk and the other one to dawn. Then, the *S* curves move sunward. Finally, the *S* curve shows a spiral with its center moving toward the Earth. The earthward movement of the *S* curve is caused by the magnetic shear associated with the large-scale field-aligned currents (FACs). One of the large-scale FACs that are responsible to the earthward movement of the *S* curve is Region 1 FACs (Iijima & Potemra, 1976), which develop for SBZ. During the expansion phase, the other Region 1-sense FACs appear in the near-Earth region in association with the near-Earth dynamo (Birn & Hesse, 2005; Ebihara & Tanaka, 2015a; Tanaka, 2015), which transport the additional electromagnetic energy to the localized region in the auroral ionosphere.

Bargatze et al. (1985) employed a linear prediction filtering technique to investigate the response of the auroral electrojet index (*AL*) and the product of solar wind velocity and SBZ. There are two responses at time lags of 20 and 60 min. They interpreted the lags as magnetospheric activity driven directly by solar wind coupling and magnetospheric activity driven by the release of energy previously stored in the tail,

respectively. The cycle of the storage and release of the magnetic energy in the lobe suggests the presence of the loading-unloading processes during the substorm (Hones, 1979; McPherron, 1970; McPherron et al., 1973). A competing idea is that the substorm is a consequence of the directly drive processes (Akasofu, 1979, 1981; Perreault & Akasofu, 1978; Tanskanen et al., 2002). This idea may be supported by the following results of statistical analyses: The *AL* index is correlated well with the parameter $B_s V_{SW}^2$ (Murayama, 1982) where *B*s is SBZ. The correlation coefficient between the ε parameter and the Joule dissipation in the ionosphere is 0.81 during the substorm expansion phase (Tanskanen et al., 2002). The argument on the dominant processes, directly driven or loading-unloading, is not fully settled. Ebihara and Tanaka (2017) performed the global MHD simulation and found that the amount of the energy released from the lobe is comparable to that continuously supplied from the solar wind. This may explain, in part, the reason why the ionospheric energy dissipation rate is correlated with the energy input rate from the solar wind. A question of what determines the amount of the magnetic energy stored in the lobe still remains.

The purpose of this study is to quantify the energy transfer from the solar wind to the ionosphere and its conversion during the substorm on the basis of the result obtained by the global MHD simulation. This paper is organized as follows. In section 2, methodology of the simulation is mentioned. In section 3, we define the substorm expansion onset, the magnetopause, and the efficient cross-sectional area in the solar wind. The simulation results are given regarding the solar wind magnetic energy and kinetic energy for different solar wind conditions. Then, we mention the magnetic energy entering the magnetosphere, the stored-and-released energy in the lobe, and the ionospheric Joule heating rate. In section 4, we discuss these results. Because of the limitation of the MHD approximation, we cannot deal with kinetic effects, such as electrons downwardly accelerated by parallel electrons. Thus, we omit the energy conversion to the kinetic energy, which is supposed to occur at low altitudes in association with bright auroras.

2. Methods

We used the global MHD simulation REPPU (REProduce Plasma Universe; Tanaka, 2015). The REPPU code is capable of reproducing many features recognized in substorms, including sudden intensification of the auroral electrojet (Tanaka, 2015), a positive bay at midlatitude (Tanaka, 2015), a westward traveling surge (Ebihara & Tanaka, 2015b; Tanaka, 2015), and counter electrojet at magnetic equator (Ebihara et al., 2014). The grid system in the magnetospheric domain is based on a triangle. First, a sphere at the inner boundary (2.6 Re) is divided into 12 pentagons. Each pentagon is further divided into 5 triangles. We call this Level 1 in which a sphere is divided into 60 triangles. We further divide the triangle into 4, which is called Level 2. In Level 2, a sphere is divided into 240 triangles. In this particular simulation, we used Level 6, in which a sphere is divided into 61,440 triangles. Three hundred twenty triangular prisms were stacked from the inner boundary outward. The number of the grid is concentrated in the plasma sheet so as to resolve the plasma sheet sufficiently. The outer boundary of the simulation domain is located at 200 Re at midnight and 600 Re at noon. This simulation couples with the ionosphere by the following means. First, we calculated the ionospheric conductivity on the basis of the FAC and the plasma pressure at the inner boundary of the simulation domain. Second, the ionospheric electric field is solved to satisfy the current continuity for given FAC and the ionospheric conductivity. Third, the ionospheric electric field is mapped from the ionosphere to the inner boundary of the magnetospheric domain located at 2.6 Re. Fourthly, the velocity corresponding to the given electric field ($=\mathbf{E}\times\mathbf{B}/B^2$) is imposed on the inner boundary of the magnetospheric domain as a boundary condition, where **E** and **B** are the electric field and the magnetic field, respectively. The detailed equation regarding the ionospheric conductivity is provided by Ebihara et al. (2014). To achieve quasi-steady state of the magnetosphere, we performed the simulation for 2 hr under the steady condition; the solar wind speed of 400 km/s, the solar wind density of 5/cm^3, IMF *B*x of 0 nT, IMF B_y of 0 nT, and IMF B_z of 3.0 nT. Then, we changed one or two parameters at 2:00 (*hour*:*minute*) as a step function in the upstream solar wind. The imposed parameters are as follows: the solar wind speed of 400, 600, and 800 km/s; the solar wind density of 5, 10, and 20/cm^3; and IMF B_z of −3, −5, and −10 nT. In total, 15 runs were performed. The parameters for the 15 runs are summarized in Table 1. Simulation results for real substorms are provided in Appendix A. A good agreement with observations is obtained in terms of auroral electrojets and Joule heating rates in the ionosphere.

Table 1
Solar Wind Velocity (V_{sw}), Solar Wind Density (N_{sw}), and IMF B_z After t = 2:00

*V*sw (km/s)	*N*sw (cm^{-3})	IMF *B*z (nT)	Name
400	5	−3	Run 1
		−5	Run 2
		−10	Run 3
600	5	−3	Run 4
		−5	Run 5
		−10	Run 6
800	5	−3	Run 7
		−5	Run 8
		−10	Run 9
400	10	−3	Run 10
		−5	Run 11
		−10	Run 12
400	20	−3	Run 13
		−5	Run 14
		−10	Run 15

3. Results

3.1. Auroral Electrojet and Definition of Expansion Onset

The auroral electrojet activity index *AE* (Davis & Sugiura, 1966) is widely used to estimate the strength of the auroral electrojet. The *AE* index is based on the variation of the *H* component taken at different magnetic local times in the auroral region. The upper and lower envelopes obtained by superposition of the *H*-component variation are called *AU* and *AL* indices, respectively. *AE* is defined by $AE = AU - AL$. The *SME* index is an extension to *AE*, which can overcome the limitation of the *AE* index, such as a problem arising from the small number of magnetometer stations used to derive the *AE* index (Newell & Gjerloev, 2011). The *SME* index is based on the magnetometer data taken at more than 100 stations. Following the concept of the *SME* index, we calculated the ionospheric Hall current and the induced magnetic disturbance on the ground at magnetic latitudes from 50° to 90° with an interval of 1° at all magnetic local times with an interval of 0.5 hr. Figure 1 shows the calculated *SMU* and *SML* indices for the 15 runs. The southward component of IMF (SBZ) arrives at the bow shock at $t \sim$ 2:05–2:07 (*hour*:*minute*) depending on the solar wind velocity. The *SML* index shows a negative excursion immediately after the increase in the solar wind dynamic pressure. This may be regarded as a substorm associated with a sudden commencement (Kawasaki et al., 1971) and is excluded in this study. We focused on the subsequent negative excursion of the *SML* index after t = 2:30 in which an apparent growth phase precedes the expansion onset. The vertical lines indicate the expansion onset time t_0 that is determined by the way proposed by Newell and Gjerloev (2011) as follows.

$$SML(t_0 + 1\ \text{min}) - SML(t_0) < -15\ \text{nT} \tag{4}$$

$$SML(t_0 + 2\ \text{min}) - SML(t_0) < -30\ \text{nT} \tag{5}$$

$$SML(t_0 + 3\ \text{min}) - SML(t_0) < -45\ \text{nT} \tag{6}$$

$$\frac{1}{26}\sum_{i=4}^{30} SML(t_0 + i\ \text{min}) - SML(t_0) < -100\ \text{nT} \tag{7}$$

It is clearly shown that the expansion onset occurs earlier when the solar wind velocity increases and SBZ increases. This is consistent with the statistical study showing that the integral substorm probability increases with the solar wind velocity and SBZ (Newell et al., 2016). The rates of change in *SML* for the first 10 min from the expansion onset are indicated by the numerical figures in each panel. The rates decrease with increasing SBZ except for the highest density case in which *SML* does not show a monotonic decrease after the expansion onset.

Figure 2 summarizes the minimum *SML* index during the period from t_0 to t_0 + 60 min for 15 runs, where t_0 is the expansion onset time determined above. There is a clear tendency that the minimum *SML* index decreases with V_{sw} and SBZ. The dependence of the minimum *SML* on N_{sw} is small. This is consistent with the statistical studies showing that *AE* depends primarily on V_{sw} and SBZ and that N_{sw} has little effect on *AE* (Maezawa, 1979; Murayama & Hakamada, 1975).

3.2. Definition of Magnetopause

To evaluate the solar wind energy transmitted to the magnetosphere (intake energy), an appropriate boundary surface, the magnetopause, must be identified. The magnetopause cannot be explicitly determined in the global MHD simulation. We identified the magnetopause as follows.

1. Trace a solar wind streamline (a line integral of the plasma velocity **V**, hereinafter called a *V* curve) from the *Y*-*Z* plane located at X = 20 Re, which is well outside of the bow shock. The start position is specified by the equations $Y = R \sin\Psi$ and $Z = R \cos\Psi$, where R is the distance from the X axis. R changes from 0 to 12 Re with a step size of 0.15 Re. ψ changes from 0 to 360° with a step size of 1°. In total, 28,800 streamlines were traced.

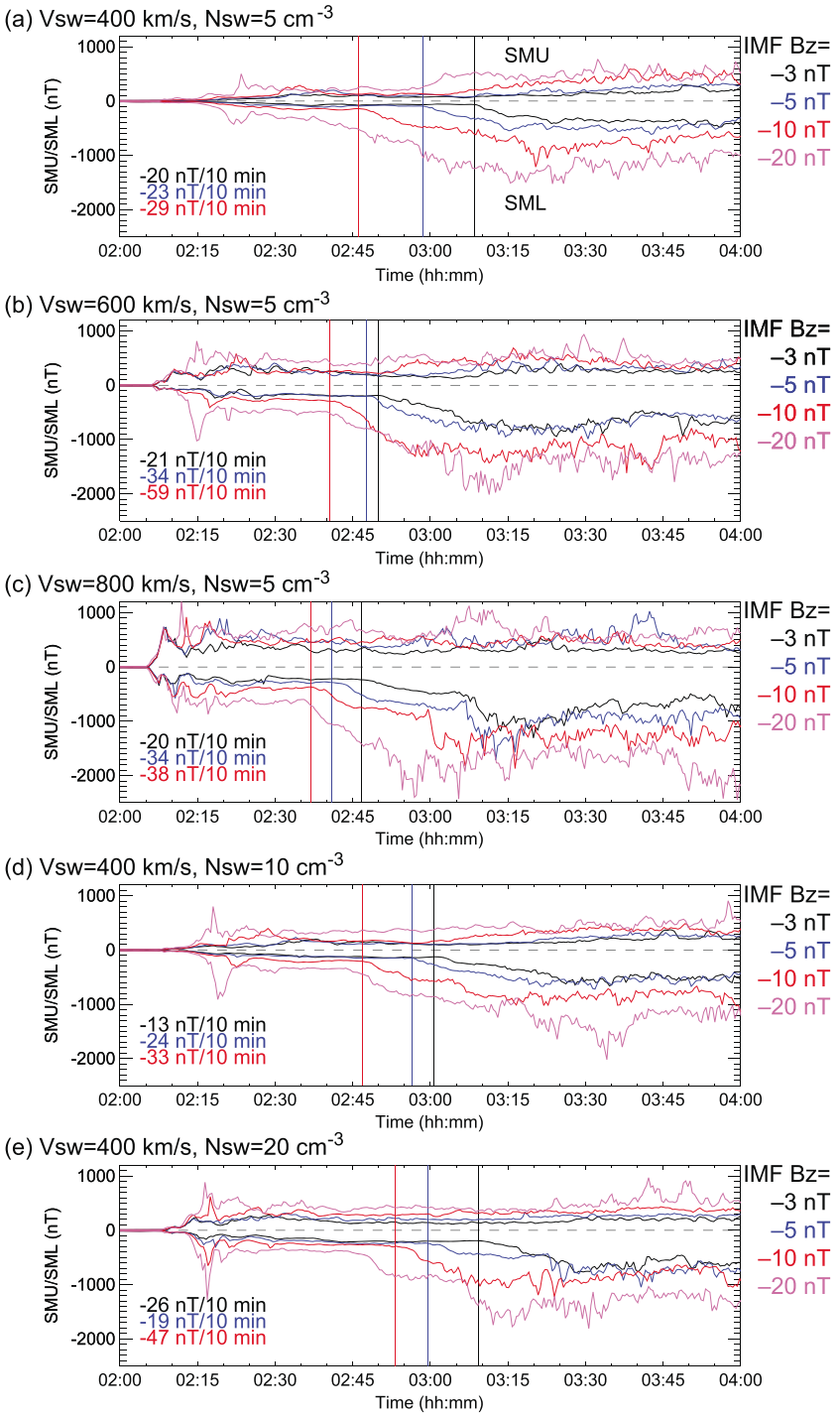

Figure 1. Simulated *SMU* and *SML* indices for 15 runs. The solid and dotted lines indicate the *SML* and the *SMU* indices, respectively. The vertical lines indicate the expansion onset time t_0 determined based on the temporal variation of the *SML* index. The numerical figures shown in each panel indicate the rate of change in *SML* for the first 10 min from the expansion onset. The *SMU* and *SML* indices for the condition that IMF $B_z = -20$ nT are added for reference.

2. Divide three-dimensional space into 0.5-Re cubes. The total number of the cubes is M.
3. Count the number of streamlines passing through each cube. Let it be N_i, where i is the cube identification number.
4. Find the maximum number of N_i as $N_{\max} = \max(N_{i\,=\,1,\,2,\,\ldots,\,M})$.

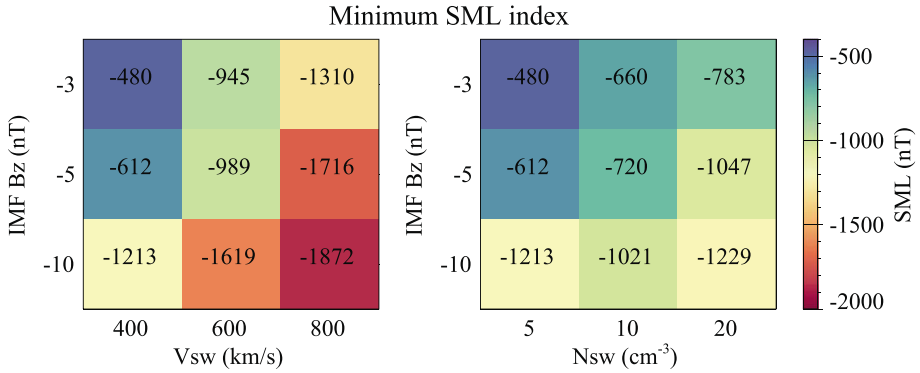

Figure 2. Minimum *SML* index within 1 hr from the onset time as a function of (left) interplanetary magnetic field (IMF) B_z and solar wind velocity V_{sw} and (right) IMF B_z and solar wind density N_{sw}.

5. Define the threshold number as $N_t = N_{max}/c$, where c is a constant and is assumed to be 200 for this particular study. The constant c may be subject to change depending on the solar wind parameters.
6. Pick up the cubes where $N_i \geq N_t$. Define the surface of the innermost cubes to be the *magnetopause*.

The search for the magnetopause is limited in the region where $X \geq -35$ Re. Figure 3 is a schematic diagram showing the geometry. The numerical figures shown in the boxes indicate examples of N_i. For this example,

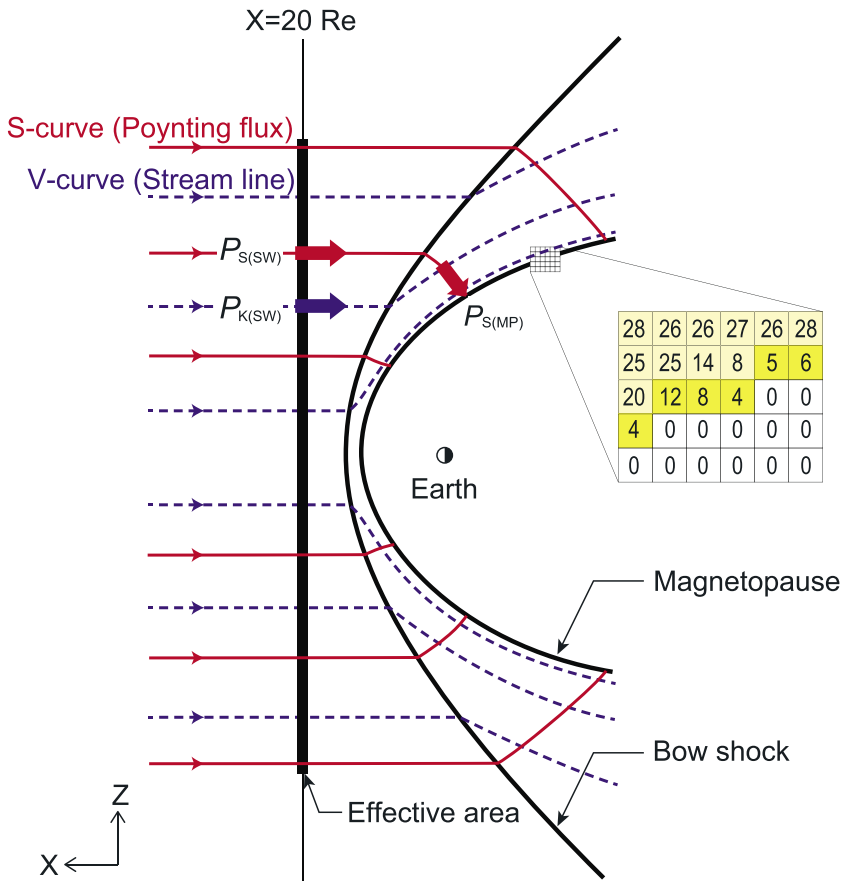

Figure 3. The magnetopause, the bow shock, and example of cubes placed in space. The red curve indicates an integral curve of the Poynting flux (*S* curve), and the blue curve indicates an integral curve of the plasma flow velocity (*V* curve). The effective cross-sectional area is located on the *Y*-*Z* plane at $X = 20$ Re. $P_{S(SW)}$, $P_{K(SW)}$, and $P_{S(MP)}$ indicate power of the solar wind magnetic flux, power of the solar wind kinetic energy, and power of the magnetic energy passing through the magnetopause, respectively.

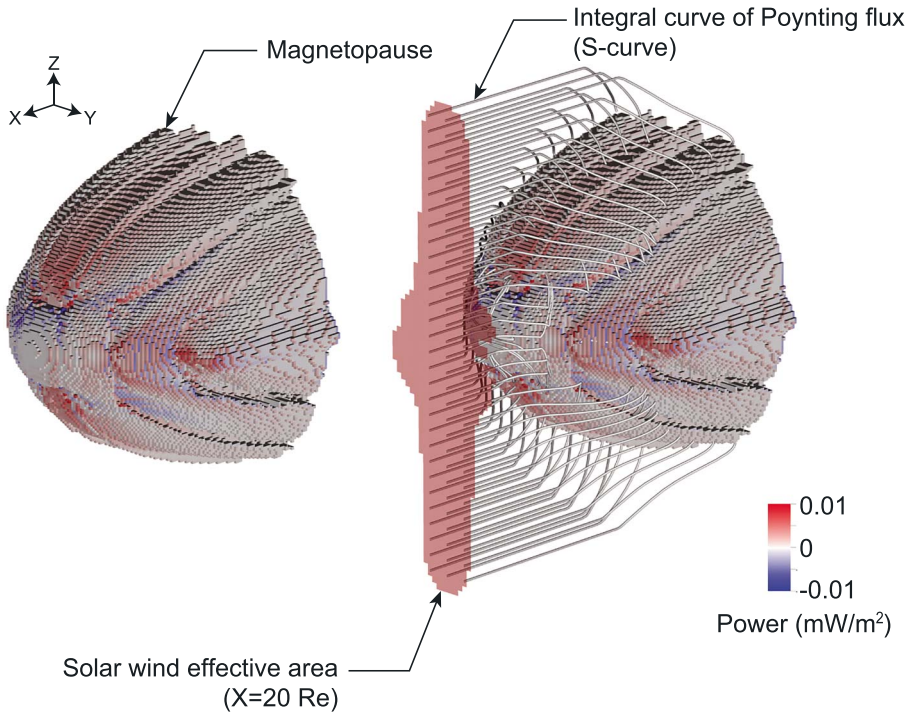

Figure 4. Magnetopause identified for Run 2 (in which $V_{sw} = 400$ km/s, $N_{sw} = 5/cm^3$, and IMF $B_z = -5$ nT) at the expansion onset. The Poynting flux is indicated on the magnetopause with color code (positive inward). The reddish plane indicates the solar wind effective area at $X = 20$ Re. The white lines indicate the integral curves of Poynting flux (S curve).

N_t is set to be 4. The yellow boxes represent the innermost cubes that indicate the magnetopause. This method is different from that suggested by Palmroth et al. (2003), who also determined the magnetopause location by the V curves. An example of the magnetopause identified by the above method is shown in the left panel of Figure 4. The color on the magnetopause indicates the Poynting flux (positive inward). The general characteristics of the distribution of the Poynting flux are similar to that obtained by Palmroth et al. (2003).

3.3. Pathway of Magnetic Energy From Solar Wind to Ionosphere

In the ideal MHD approximation, three types of energy can be defined, namely, the electromagnetic energy, the kinetic energy, and the internal energy (Birn & Hesse, 2005). According to Poynting's theorem, the continuity equation for the electromagnetic energy is given by

$$\frac{\partial}{\partial t}\left(\frac{B^2}{2\mu_0}\right) + \nabla\cdot\mathbf{S} = -\mathbf{J}\cdot\mathbf{E}, \tag{8}$$

where $\mathbf{S}$ is the Poynting flux ($=\mathbf{E}\times\mathbf{B}/\mu_0$), μ_0 is the magnetic constant, and $\mathbf{J}$ is the current density. The term related to the electric energy is omitted. Hereinafter, we reword the electromagnetic energy by the magnetic energy because the magnetic energy dominates the electric energy in the MHD approximation. The continuity equation for the kinetic energy is given by

$$\frac{\partial}{\partial t}\left(\frac{\rho}{2}V^2\right) + \nabla\cdot\left(\frac{\rho}{2}V^2\mathbf{V}\right) = \mathbf{V}\cdot(\mathbf{J}\times\mathbf{B} - \nabla P), \tag{9}$$

where ρ is the mass density of plasma and P is the plasma pressure. The continuity equation for the internal energy is given by

$$\frac{\partial u}{\partial t} + \nabla\cdot(\gamma u\mathbf{V}) = \mathbf{V}\cdot\nabla P, \tag{10}$$

where u and γ is the thermal energy density of plasma ($=3p/2$) and the ratio of specific heat ($=5/3$), respectively. Readers may refer to Birn and Hesse (2005) and Ebihara and Tanaka (2017) for the

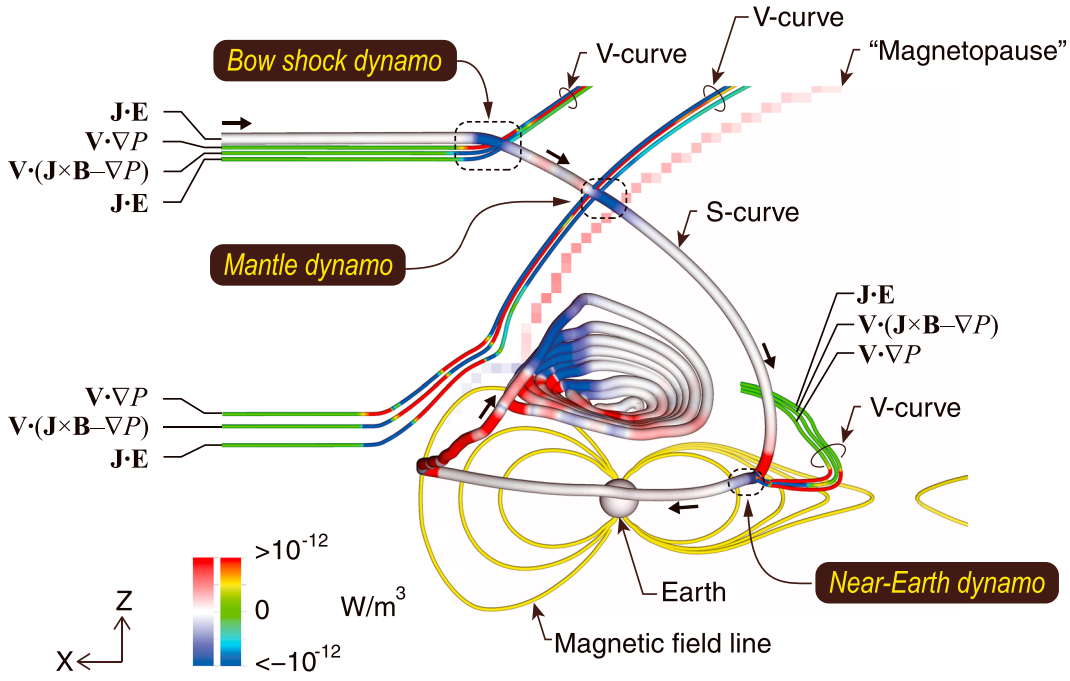

Figure 5. Line integral of the Poynting flux (*S* curve; whitish, thick line) and line integral of flow velocity (*V* curve; thin line) at expansion onset for Run 2. The color code on the *S* curve indicates $\mathbf{J} \cdot \mathbf{E}$ and that on the *V* curve indicates $\mathbf{V} \cdot \nabla P$, $\mathbf{V} \cdot (\mathbf{J} \times \mathbf{B} - \nabla P)$, and $\mathbf{J} \cdot \mathbf{E}$. The yellow line indicates the magnetic field line. The sphere indicates the Earth.

derivation of equations (9) and (10). The energy conversion takes place through the right-hand sides of equations (8)–(10).

Figure 5 shows integral curves of the Poynting flux $\mathbf{S}$ (*S* curve) and flow velocity $\mathbf{V}$ (*V* curve) at the expansion onset for Run 2. The color code of the *S* curve represents $\mathbf{J} \cdot \mathbf{E}$, and the color codes of the *V* curves represent $\mathbf{V} \cdot \nabla P$, $\mathbf{V} \cdot (\mathbf{J} \times \mathbf{B} - \nabla P)$, and $\mathbf{J} \cdot \mathbf{E}$. The *S* curve starts at $X = 20$ Re in the solar wind. As the *S* curve encounters the bow shock, it undergoes the first dynamo region where $\mathbf{J} \cdot \mathbf{E} < 0$ (bow shock dynamo). Three *V* curves passing through near the bow shock dynamo indicate the conversion from the kinetic energy to the magnetic energy and the internal energy (in which $\mathbf{V} \cdot (\mathbf{J} \times \mathbf{B} - \nabla P) < 0$, $\mathbf{J} \cdot \mathbf{E} < 0$, and $\mathbf{V} \cdot \nabla P > 0$). After the passage of the bow shock, the *S* curve is deflected toward the equatorial plane of the magnetosphere. The *S* curve passes through the second dynamo region just outside the magnetopause, which is called a mantle dynamo (Tanaka, 2000, 2007). According to the color codes on the *V* curves passing through the mantle dynamo, the conversion from the internal energy to the magnetic energy and the kinetic energy is identified (in which $\mathbf{V} \cdot \nabla P < 0$, $\mathbf{J} \cdot \mathbf{E} < 0$, and $\mathbf{V} \cdot (\mathbf{J} \times \mathbf{B} - \nabla P) > 0$). This conversion is also demonstrated by Tanaka et al. (2016). The *S* curve traverses the magnetopause defined above and moves toward the equatorial plane. The *S* curve undergoes the third dynamo region in the near-Earth region, which is called a near-Earth dynamo (Ebihara & Tanaka, 2015a; Tanaka, 2015). The conversion from the internal energy to the kinetic energy and the magnetic energy is found (in which $\mathbf{V} \cdot \nabla P < 0$, $\mathbf{J} \cdot \mathbf{E} < 0$, and $\mathbf{V} \cdot (\mathbf{J} \times \mathbf{B} - \nabla P) > 0$). It is also shown that the magnetic energy in the lobe is converted to the internal energy consumed in the near-Earth dynamo. The conversion of the energy in the near-Earth dynamo is also mentioned by Birn and Hesse (2005) and Ebihara and Tanaka (2017) in detail. The *S* curve travels sunward, and subsequently, it shows a spiral with its center moving toward the Earth. The center of the spiral moves toward the ionosphere because of the magnetic shear, that is, the presence of the large-scale FACs.

Figure 6 shows $\partial/\partial t(B^2/2\mu_0)$in the meridional plane for Run 2. About 5 min before the onset, the value is positive in the almost entire region of the lobe, which means that the magnetic energy is stored in the growth phase. The value is negative near the equatorial plane at $X \sim -13$ Re in association with the formation of near-Earth reconnection. (The near-Earth reconnection takes place closer to the Earth in comparison with most of the observations; Angelopoulos et al., 2008; Nagai et al., 1998. In the global MHD simulation, the near-Earth reconnection takes place at ~$X \sim -17$ Re; Tanaka et al., 2017, and $X \sim -42$ Re; Ebihara &

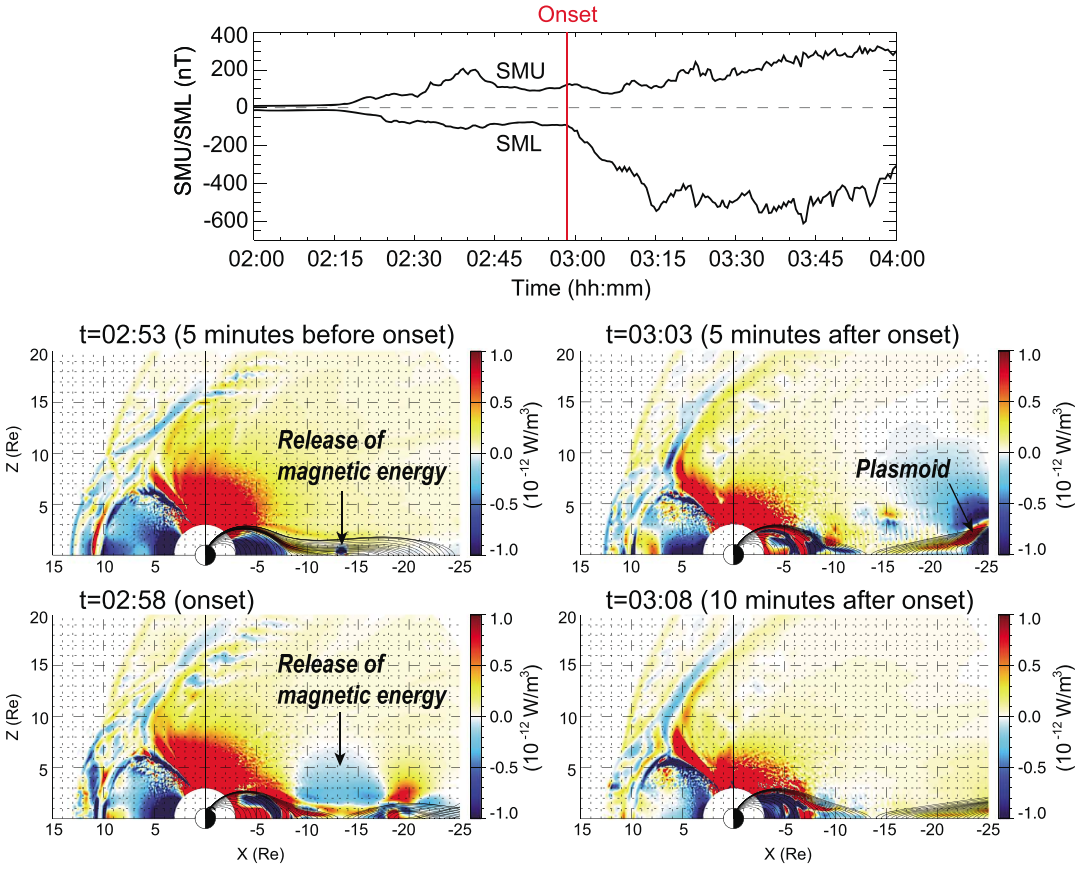

Figure 6. (top) *SMU* and *SML* indices and (bottom) time derivative of the magnetic energy in the meridional plane for Run 2.

Tanaka, 2015b, depending on the solar wind parameters and simulation settings. We believe that the location of the near-Earth reconnection is not far from reality because Sergeev et al., 2008, observed the near-Earth reconnection at 9–13 Re. We confirmed that the physical processes leading to the substorm are essentially the same regardless of the location of the near-Earth reconnection.) At onset, the value is negative in the lobe region above the near-Earth reconnection at $|Z| < \sim 7$ Re. This is a clear indication of the release of the magnetic energy previously stored in the lobe. The *S* curve shown in Figure 5 does not pass through the negative-value region. About 5 min after the onset, the negative-value region that is evident at the onset almost disappears. Instead, another negative-value region appears in the vicinity of the plasmoid. The negative-value region has gone by about 10 min after the onset. It is interesting to point out that the auroral electrojet seen by the *SML* index keeps decreasing at least for ~15 min from the onset. The release of the magnetic energy seems to end by ~10 min from the onset, much earlier than the end of the expansion phase. It may take, at least, several minutes to propagate energy from the lobe to the ionosphere. Thus, it is too early to conclude that the development of the auroral electrojet is not fully sustained by the energy stored in the lobe. Further studies are needed to conclude this.

3.4. Original Amount of Solar Wind Energy

The ultimate source of the energy consumed in the ionosphere is the solar wind. To evaluate the original amount of the solar wind energy that enters the magnetosphere, we defined an effective cross-sectional area in the solar wind. The effective area is an area in which all the Poynting fluxes entering the magnetosphere pass through. The method to identify the solar wind effective area is summarized as follows:

1. Divide the *Y*-*Z* plane located at $X = 20$ Re into 1-Re squares.
2. Trace the *S* curve backward from the magnetopause until it reaches the *Y*-*Z* plane located at $X = 20$ Re.
3. Count the number of the *S* curves passing through each square.

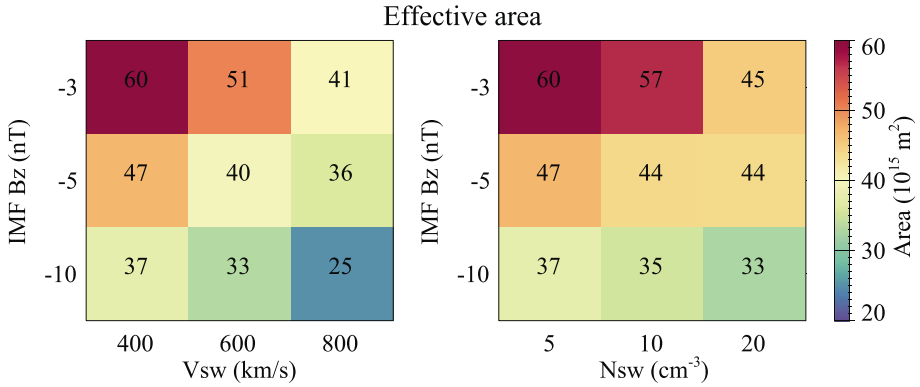

Figure 7. Solar wind effective area A_{eff} as a function of V_{sw}, N_{sw}, and IMF B_z.

4. Define the region where the number is greater than 0 to be the solar wind effective area.

An example of the solar wind effective area is shown by the reddish plane in the right panel of Figure 4, indicating that all the Poynting flux connecting to the magnetopause passes through the effective area. Figure 7 summarizes the solar wind effective area A_{eff} for the 15 runs. The effective area decreases with V_{sw} and N_{sw}, which is attributed to the contract of the magnetosphere owning to the increase in the solar wind dynamic pressure. The effective area also decreases with SBZ probably due to the draping of the IMF.

Figure 8 summarizes power of the solar wind magnetic energy and kinetic energy passing through the effective area in the solar wind A_{eff}. The power of the solar wind magnetic energy $P_{S(SW)}$ is given by

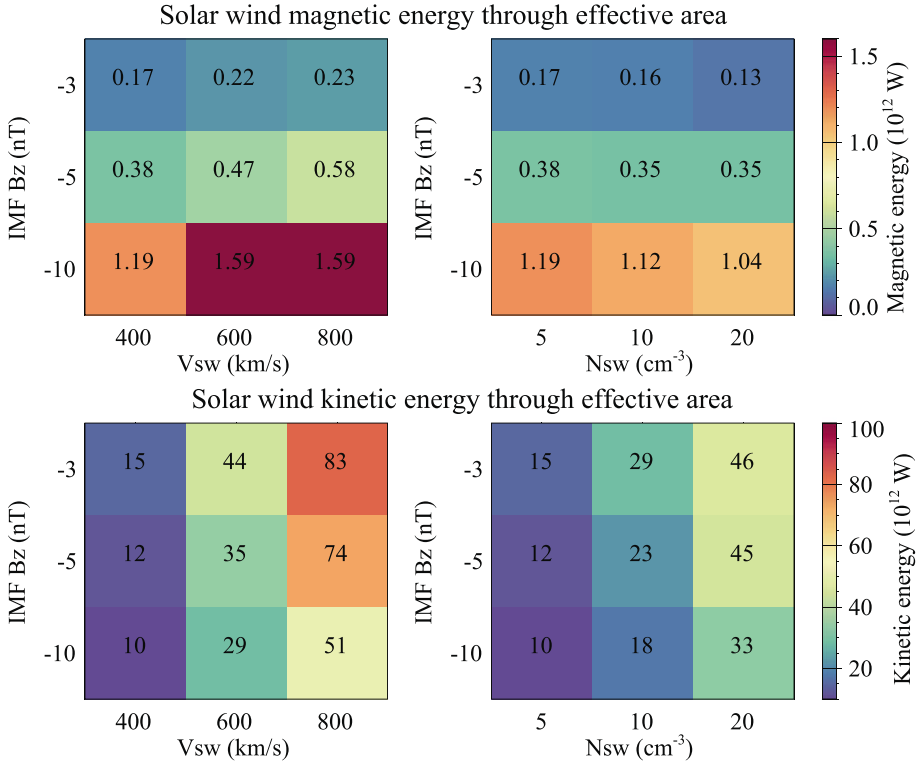

Figure 8. (top) Power of solar wind magnetic energy $P_{S(SW)}$ and (bottom) power of kinetic energy $P_{K(SW)}$ passing through the effective area A_{eff}.

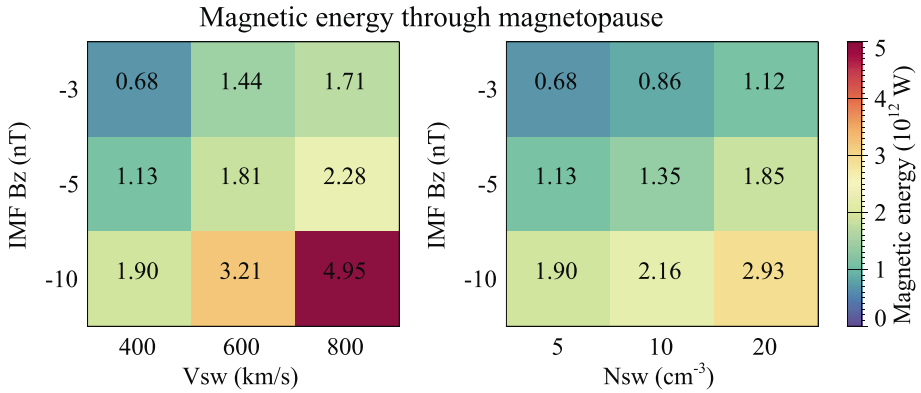

Figure 9. Magnetic energy passing through the magnetopause per unit time $P_{S(MP)}$.

$$P_{S(SW)} = \int \mathbf{S} \cdot d\mathbf{A} = SA_{eff}, \tag{11}$$

where $d\mathbf{A}$ is the normal surface vector. As shown in the top panel of Figure 8, $P_{S(SW)}$ increases with B_s, while the dependence on V_{sw} and N_{sw} is weak. One prime reason for the weak dependence is the decrease in A_{eff} with V_{sw} and N_{sw}.

The power of the solar wind kinetic energy $P_{K(SW)}$ is calculated by

$$P_{K(SW)} = \int \frac{1}{2} m N_{sw} {V_{sw}}^2 \mathbf{V}_{sw} \cdot d\mathbf{A} = \frac{1}{2} m N_{sw} {V_{sw}}^3 A_{eff}, \tag{12}$$

where m is the mass of the solar wind (which is assumed to be 1.6×10^{-27} kg). As shown in the bottom panel of Figure 8, $P_{K(SW)}$ increases with V_{sw} and N_{sw}. $P_{K(SW)}$ decreases with SBZ because of the decrease in the effective area with SBZ. $P_{K(SW)}$ is more than 1 order of magnitude larger than $P_{S(SW)}$. For example, for Run 1 (IMF $B_z = -3$ nT, $V_{sw} = 400$ km/s, and $N_{sw} = 5/\text{cm}^3$), $P_{K(SW)}$ is about 88 times larger than $P_{S(SW)}$.

3.5. Energy Penetrating Into Magnetosphere

Knowing the location and the normal vector of the magnetopause, we can calculate the magnetic energy passing through the magnetopause per unit time as

$$P_{S(MP)} = \int \mathbf{S} \cdot d\mathbf{A}. \tag{13}$$

The results are summarized in Figure 9. The power passing through the magnetopause increases with V_{sw}, N_{sw}, and SBZ. The influence of N_{sw} on the power is smaller than that of V_{sw} and SBZ. It is noted that $P_{S(MP)}$ is much larger than $P_{S(SW)}$ (original amount of power of the magnetic energy passing through the solar wind effective area). This means that the solar wind magnetic energy is insufficient to supply the magnetic energy entering the magnetosphere. Conversion from the solar wind kinetic energy to the magnetic energy is necessary before reaching the magnetopause. It is noted that the kinetic energy passing through the magnetopause is very small and negligible as compared with the magnetic energy.

Figure 10 shows the ratio of $P_{S(SW)}$ (original amount of the magnetic energy passing through the solar wind effective area per unit time) to $P_{S(MP)}$ (total amount of magnetic energy passing through the magnetopause per unit time) for 15 runs. The ratio is much smaller than 1. Again, this indicates that the solar wind magnetic energy is insufficient to supply the magnetic energy entering the magnetosphere. For Run 1 (IMF $B_z = -3$ nT, $V_{sw} = 400$ km/s, and $N_{sw} = 5/\text{cm}^3$), the ratio is 0.25, meaning that ~25% of $P_{S(MP)}$ comes from $P_{S(SW)}$ and that ~75% of $P_{S(MP)}$ must be converted from the solar wind kinetic energy $P_{K(SW)}$. (The internal energy of the solar wind is negligible.) It is noted that the ratio is almost 1 for northward IMF (data not shown), meaning that $P_{S(SW)}$ is almost sufficient to supply energy to $P_{S(MP)}$ and that the contribution from

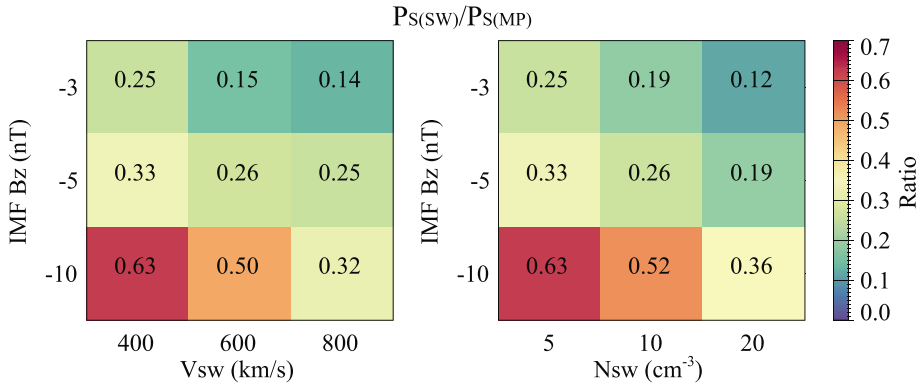

Figure 10. Ratio of $P_{S(SW)}$ to $P_{S(MP)}$.

$P_{K(SW)}$ is very minor for northward IMF. This is simply understood to the absent of the mantle dynamo for northward IMF (Tanaka, 1995).

Figure 11 presents the ratio $(P_{S(MP)} - P_{S(SW)})/P_{K(SW)}$ that means the relative contribution from the solar wind kinetic energy to intake magnetic energy. In other word, this ratio is regarded as a proxy for the efficiency of the bow shock/mantle dynamos. For Run 1 (IMF $B_z = -3$ nT, $V_{sw} = 400$ km/s, and $N_{sw} = 5$/cm^3), about 2–7% of the solar wind kinetic energy is converted to the magnetic energy penetrating into the magnetosphere. There is a tendency that this ratio decreases with V_{sw} and N_{sw}.

3.6. Storage and Release of Magnetic Energy in Lobe

The characteristics of storage and release of the magnetic energy in the lobe can be represented by the rate of the change in the magnetic energy as

$$P_{S(LOBE)} = \int \frac{\partial}{\partial t}\left(\frac{B^2}{2\mu_0}\right) dV. \tag{14}$$

Positive (negative) $P_{S(LOBE)}$ value means that the magnetic energy is stored (released). Figure 12 shows the maximum $P_{S(LOBE)}$ during the period from t_0–30 min and t_0 (growth phase) and the minimum $P_{S(LOBE)}$ during the period from t_0 and t_0 + 60 min (expansion phase). The power is calculated by integrating the rate of the change in the magnetic energy over the rectangular volume (X ranging from −20 to −10 Re, Y ranging from −3 to 3 Re, and Z ranging from 4 Re to 15 Re). The integration range in the X direction is the same as that used by Akasofu (2013). There are three points to be noted. First, the amplitude of the maximum released power is slightly larger than, or almost comparable to that of the stored power. Second, both the stored power and the released power tend to increase with V_{sw}, N_{sw}, and SBZ. Third, the dependence on N_{sw} is large. The result implies that both the stored power and the released power in the lobe are regulated by the solar wind condition.

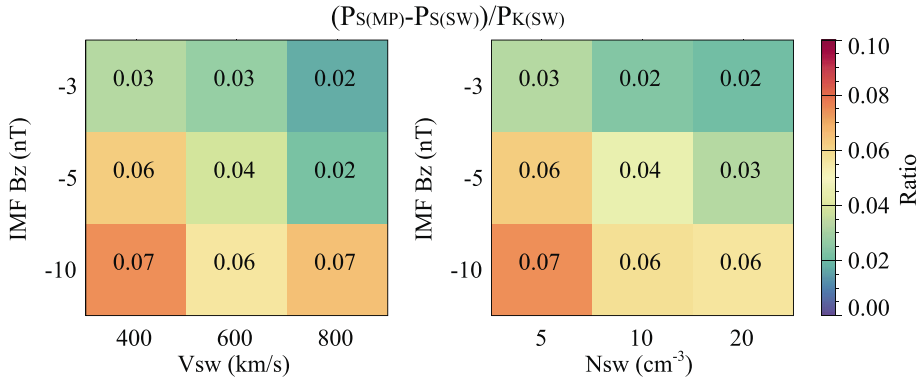

Figure 11. The $(P_{S(MP)} - P_{S(SW)})/P_{K(SW)}$ratio, which indicates relative contribution from solar wind kinetic energy to the solar wind magnetic energy entering the magnetosphere per unit time.

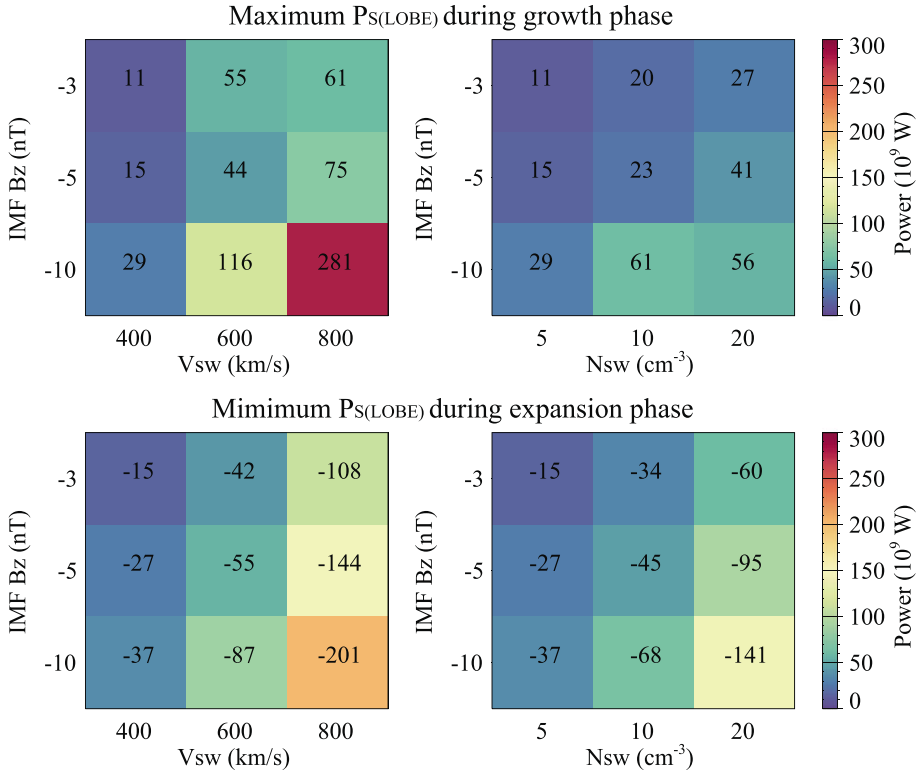

Figure 12. (top) Maximum $P_{S(LOBE)}$ during the growth phase (from t_0–30 min to t_0) and (bottom) minimum $P_{S(LOBE)}$ during the expansion phase (from t_0 to t_0 + 60 min). Only the Northern Hemisphere is considered.

3.7. Energy Consumption in Ionosphere

Figure 13 shows the hemispheric Joule heating rate in the ionosphere, which is calculated as

$$P_{S(IS)} = \int \mathbf{j}\cdot\mathbf{E}dA, \qquad \mathbf{j} = \Sigma_p \mathbf{E}, \tag{15}$$

where Σ_p is the height-integrated Pedersen conductivity and $\mathbf{j}$ is the electric current density in the ionosphere. The top panels show the Joule heating rate at the expansion onset, which increases with V_{sw}, N_{sw}, and SBZ. The influence of V_{sw} and SBZ on the maximum Joule heating rate is large, whereas the dependence of N_{sw} is small. The bottom panels show the maximum Joule heating rate during the expansion phase (from t_0 to t_0 + 60 min), indicating the similar tendency except for the dependence on N_{sw}. The dependence of the maximum Joule heating rate on N_{sw} is very weak. This result is consistent with the study by Tanskanen et al. (2002).

The maximum Joule heating rate during the expansion phase is comparable to the maximum power released from the lobe as shown in Figure 12. For some runs, the maximum Joule heating rate is smaller than the maximum power released from the lobe (Runs 3, 4, 5, 6, and 8). This is not a surprising result because the contribution from the magnetic energy directly supplied from the solar wind is significant and is comparable to that released from the lobe (Ebihara & Tanaka, 2017).

3.8. Solar Wind-Ionosphere Coupling

Figure 14 represents the relationship between $P_{S(MP)}$ (the total amount of power of the magnetic energy penetrating into the magnetosphere) and the ε parameter. Roughly speaking, $P_{S(MP)}$ is larger than the ε parameter by a factor of 3 and 4. This is consistent with the previous simulation result (Palmroth et al., 2003). One of the plausible reasons is underestimation of the ε parameter. The ε parameter was derived based on the Poynting flux in interplanetary space, so that the conversion from the solar wind kinetic energy is not

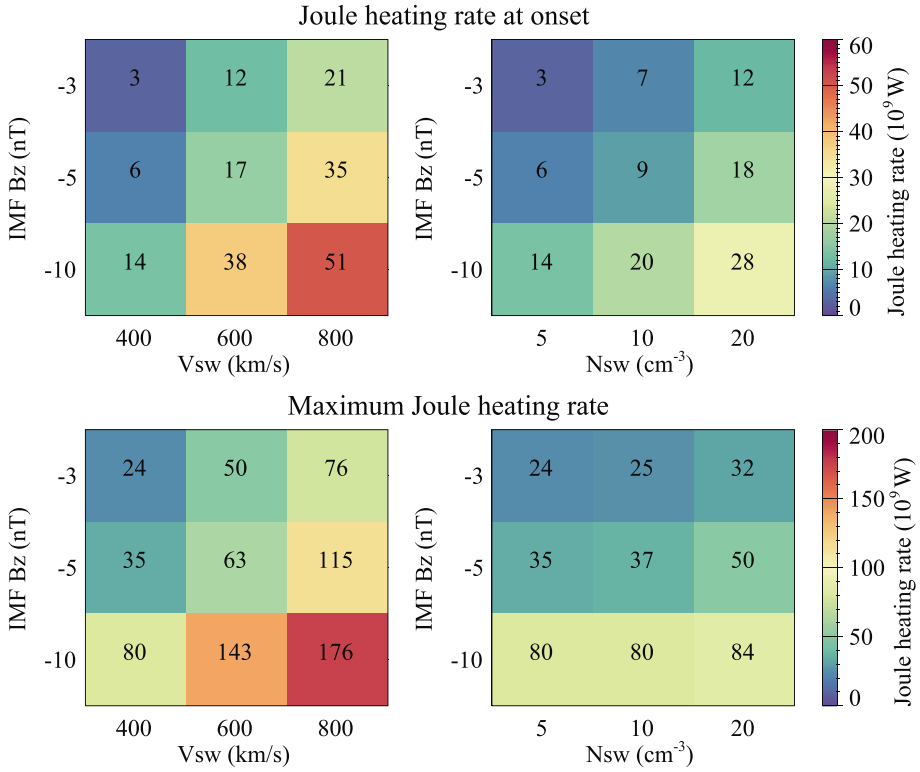

Figure 13. (top) Joule heating rate in the ionosphere (one hemisphere) at the expansion onset, and (bottom) maximum Joule heating rate from the expansion onset to 60 min after the onset. Only the Northern Hemisphere is considered.

explicitly considered. With this regard, the underestimation may come from the exclusion of the contribution from the solar wind kinetic energy. Perreault and Akasofu (1978) originally assumed the length l_0 in equations (1) and (2) to be 7 Re. Recently, Akasofu (2017) suggested the length l_0 to be 15 Re for geomagnetic storms. Replacing the length l_0 of 7 Re by that of 15 Re, one may almost resolve the discrepancy between $P_{S(MP)}$ and the ε parameter. The ε parameter will be still valid for estimating roughly the incoming magnetic energy into the magnetosphere if the length l_0 is properly (or arbitrarily) chosen. In this case, the length l_0 will be meant to include the contribution from the solar wind kinetic energy and will be probably regarded as a magic number, which includes relevant physical processes involved in energy transfer from the solar wind to the magnetosphere as suggested by this study.

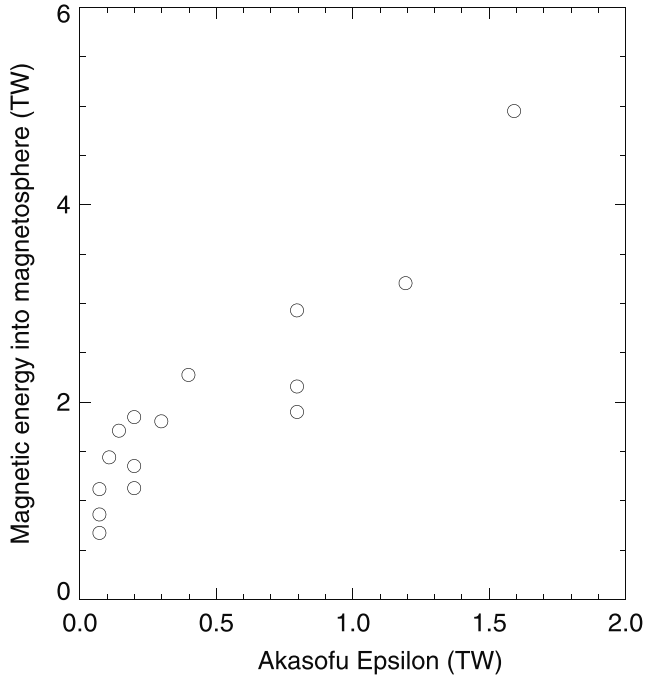

Figure 14. Magnetic energy entering the magnetosphere per unit time ($P_{S(MP)}$) versus ε.

Table 2 summarizes correlation coefficients of ε, $P_{K(SW)}$, $P_{S(SW)}$, and $P_{S(MP)}$ with minimum *SML*, the ionospheric Joule heating rate at onset, and the maximum ionospheric Joule heating rate during the expansion phase (t_0 and t_0 + 60 min). The best correlation is found for $P_{S(MP)}$, suggesting that ε is better than $P_{S(MP)}$ in determining the minimum *SML* and the maximum ionospheric Joule heating rate. The correlation between $P_{K(SW)}$ and the ionospheric parameters is poor, which has already been pointed out by Akasofu (1981).

3.9. Northward IMF

Finally, we mention the result for northward IMF. We imposed the following parameters, V_{sw} of 400 km/s, N_{sw} of 5/cm^3, and IMF B_z of 3.0 nT to the upstream solar wind to the simulation until t = 2:00 to establish the quasi-steady magnetosphere. At t = 2:00, the magnetosphere is

Table 2
Correlation Coefficients With Minimum SML, Ionospheric Joule Heating Rate at Onset, and Maximum Ionospheric Joule Heating Rate From the Expansion Onset to 60 Min After the Onset

Type of power	Minimum *SML*	Joule heating rate at onset	Maximum Joule heating rate
Perreault and Akasofu's ε	−0.74	0.77	0.90
Kinetic energy in solar wind $P_{K(SW)}$	−0.53	0.53	0.28
Magnetic energy in solar wind $P_{S(SW)}$	−0.69	0.70	0.87
Magnetic energy into magnetosphere $P_{S(MP)}$	−0.90	0.93	0.97

exposed to northward IMF. The effective area is ~11×10^{15} m^2, which is about 18% of that in the SBZ case (Run 1, V_{sw} of 400 km/s, N_{sw} of 5/cm^3, and IMF B_z of −3.0 nT after t = 2:00). $P_{S(SW)}$ is ~0.086×10^{12} W, which is about half of that in the SBZ case. $P_{K(SW)}$ is ~2.8×10^{12} W, which is ~19% of that in the SBZ case. $P_{S(MP)}$ is ~0.079×10^{12} W, which is ~12% of that in the SBZ case, and is comparable to $P_{S(SW)}$. This means that the solar wind kinetic energy is not efficiently converted to the magnetic energy for the northward IMF case.

4. Discussion

The above results show that in addition to the contribution from the solar wind magnetic energy, the contribution from the solar wind kinetic energy is significant for the southward IMF case. The power of the solar wind kinetic energy is proportional to N_{sw}, but the intake magnetic energy per unit time ($P_{S(MP)}$) shows a weak dependence on N_{sw}. The reasons may be summarized as follows. First, the solar wind effective area decreases with N_{sw} (Figure 7). Second, the original amount of the power of the solar wind magnetic energy decreases with N_{sw} (Figure 8), resulting from the decrease in the effective area. Third, the relative contribution from the solar wind kinetic energy to $P_{S(MP)}$ decreases with N_{sw} (Figure 11). The combination of these factors is thought to give rise to the weak dependence of N_{sw} on $P_{S(MP)}$.

Based on global MHD simulation results, Wang et al. (2014) suggested that the energy coupling function between the solar wind and the magnetosphere is proportional to $N_{sw}{}^{0.24}V_{sw}{}^{1.47}B^{0.86}$. The complicated form of the coupling function can be reasonably explained by the contribution from the two types of energy flux (magnetic energy flux being proportional to $V_{sw}B^2$ and kinetic energy flux being proportional to $N_{sw}V_{sw}{}^3$). The dependence of the effective area on the solar wind parameters also makes the coupling function complicated. Wang et al. (2014) also estimated that about 13% of the solar wind kinetic energy is transferred into the magnetosphere. This is different from our results that about 2–7% of the solar wind kinetic energy appears to be converted to the magnetic energy that enters the magnetosphere as shown in Figure 11. The difference may come from the difference of the definition. They calculated the ratio such as $P_{S(MP)}/P_{K(SW)}$ to show the efficiency of the conversion from the solar wind kinetic energy to the intake magnetic energy. However, the original contribution from the solar wind magnetic energy is neglected. The ratio $(P_{S(MP)} - P_{S(SW)})/P_{K(SW)}$seems to be better for describing the efficiency as we introduced. Wang et al. (2014) used the maximum cross section of the magnetopause to calculate $P_{K(SW)}$. However, use of the maximum cross section of the magnetopause is improper to evaluate the solar wind energy input because the cross section of the magnetopause is totally different from the solar wind effective area as shown in Figure 4.

Tanskanen et al. (2002) showed that the correlation coefficient between energy input into the magnetosphere and the ionospheric Joule dissipation is 0.81 during the expansion phase of an isolated substorm. They used the ε parameter to evaluate the energy input into the magnetosphere. The result is consistent with our results. As shown in Table 2, the correlation coefficient between the ε parameter and the maximum Joule heating rate is 0.90. The correlation coefficient is found to increase to 0.97 when $P_{S(MP)}$ is used. Tanskanen et al. (2002) also pointed out that the directly driven processes are important for the ionospheric Joule dissipation because the energy input and the Joule dissipation are well correlated. Our global MHD simulation results also show that they are well correlated. There are two prime reasons for the high correlation. First, the magnetic energy stored in the lobe is not only the energy source that is consumed in the ionosphere. A large amount magnetic energy originating from the solar wind is continuously and directly supplied toward the plasma sheet during the expansion phase (Ebihara & Tanaka, 2017). Second, the rates of the

magnetic energy stored in the lobe and released from the lobe depend on the solar wind parameters, V_{sw}, N_{sw}, and SBZ. These two results imply that both the directly driven and the loading-unloading processes depend on the solar wind parameter. This may explain the reason that the good correlation between the intake magnetic energy and the Joule dissipation is achieved. It is noted that the good correlation between a certain parameter and the energy input does not always mean the dominance of the directly driven processes. That is because, as shown Figure 12, the energy released from the lobe is regulated by the solar wind parameters.

A part of the energy entering the magnetosphere is thought to escape from the system as a plasmoid (Baker et al., 1997; Hones et al., 1984). The magnetic energy, the internal energy, and the kinetic energy extracted from the system as a plasmoid are estimated to be 1.6×10^{13} J, 2.3×10^{14} J, and 1×10^{14} J, respectively, for a typical plasmoid (Hesse, 1995). Baker et al. (1997) estimated the amount of energy loss due to the ejection of the plasmoid is 10^{11}–10^{12} W. To estimate the amount of the energy loss due to the ejection of the plasmoid, a careful integration is needed. Our intension, in this particular paper, is to evaluate the amount of the energy that is fed into the ionosphere. For a reference, we calculated the magnetic energy escaping from the magnetotail in the *Y*-*Z* plane at $X = -35$ Re at the expansion onset. The magnetic energy escaping from the magnetotail is the same order of magnitude as that released from the lobe (not shown). This is understandable because of the following reasons. First, both the energy released from the lobe and the energy directly supplied from the solar wind are comparable. Second, the energy passing through the magnetic separatrix from the open region (lobe) to the closed region splits into the earthward energy and the antiearthward energy.

The inner boundary of the magnetospheric domain is located at 2.6 Re. We did not solve the gap between the inner boundary of the simulation domain and the ionosphere. During the substorm expansion phase, a large number of electrons are known to be accelerated downward by quasi-electrostatic electric field along a field line. The parallel electric field is probably extended at altitude greater than 3 Re (Mozer & Hull, 2001). When the parallel electric field is present, the electromagnetic energy is converted to the kinetic energy (Song & Lysak, 2001), which contributes to the heating of the ionosphere. According to the statistical study, the kinetic energy flux is largely enhanced near midnight during magnetically active time as compared with the Poynting flux (Cosgrove et al., 2014). The energy flow and the distribution factors at low altitude are still controversial. Ahn et al. (1983) estimated that the particle energy injection rate into the ionosphere is about one fourth of the Joule dissipation rate. The conversion of the energy at low altitude must be solved and be taken into consideration in the global simulation in the future to evaluate the overall energy flow.

We cannot rule out the possibility that non-MHD plasma instability leads to and sustain the substorm expansion. The plasma instability can explain the disruption of the cross-tail current (Cheng & Lui, 1998; Lui et al., 1990), but it is uncertain if the plasma instability can sustain the large-amplitude FACs that manifest the substorm expansion phase. A full Vlasov simulation or a full particle simulation will be necessary to verify the role of the non-MHD plasma instability.

5. Conclusions

On the basis of the global MHD simulation results, we reached the following conclusions regarding the energy transfer from the solar wind to the ionosphere.

1. Minimum *SML* index (which is an extension of the *AL* index) during the expansion phase decreases with southward component of IMF (SBZ) and solar wind velocity (V_{sw}). The dependence of the minimum *SML* index on the solar wind density (N_{sw}) is weak. These features are consistent with the observations.
2. We defined the solar wind effective cross-sectional area in which all the integral curves of the Poynting flux (*S* curve) entering the magnetosphere pass through. About 33–88% of the magnetic energy entering the magnetosphere ($P_{S(MP)}$) is converted from the solar wind kinetic energy. About 2–7% of the solar wind kinetic energy (passing through the effective area) is converted to the magnetic energy that enters the magnetosphere. Both the solar wind magnetic energy and the solar wind kinetic energy are the prime sources for the intake magnetic energy into the magnetosphere for southward IMF.
3. For southward IMF, the effective area decreases with SBZ, V_{sw}, and N_{sw}. $P_{S(MP)}$ increases with B_s, V_{sw}, and N_{sw}, but its dependence on N_{sw} is weak. This is consistent with previously suggested energy coupling functions.

4. $P_{S(MP)}$ is proportional to neither $V_{sw}B^2$ (Poynting flux) nor $N_{sw}V_{sw}^3$ (kinetic energy flux). The complexity, which is consistent with previous studies, comes from the combination of the Poynting flux and the kinetic energy flux as well as the effective area depending on the solar wind parameters.
5. The ionospheric Joule heating rate increases with SBZ and V_{sw} and is well correlated with $P_{S(MP)}$ at onset (correlation coefficient of 0.93) as well as during the substorm expansion (correlation coefficient of 0.97). It seems that both the directly driven and unloading processes depend on the solar wind condition. A good correlation between some parameter and the energy input does not always mean the dominance of the directly driven process.
6. The rates of the magnetic energy stored in the lobe and released from the lobe depend on the solar wind parameters, SBZ, V_{sw}, N_{sw}. This can explain the reason why the ionospheric Joule dissipation is well correlated with the intake magnetic energy.
7. For northward IMF, $PS(MP)$ is small because the effective area is small, and the solar wind kinetic energy is not efficiently converted to the magnetic energy outside the magnetopause.

Appendix A

To show the quality of the simulation results, we performed the global MHD simulation for the substorms that occurred on 28–29 March 1998. Solar wind and IMF data from the OMNI database with a resolution of 1 min (King & Papitashvili, 2005) are used to provide the boundary condition of the global MHD

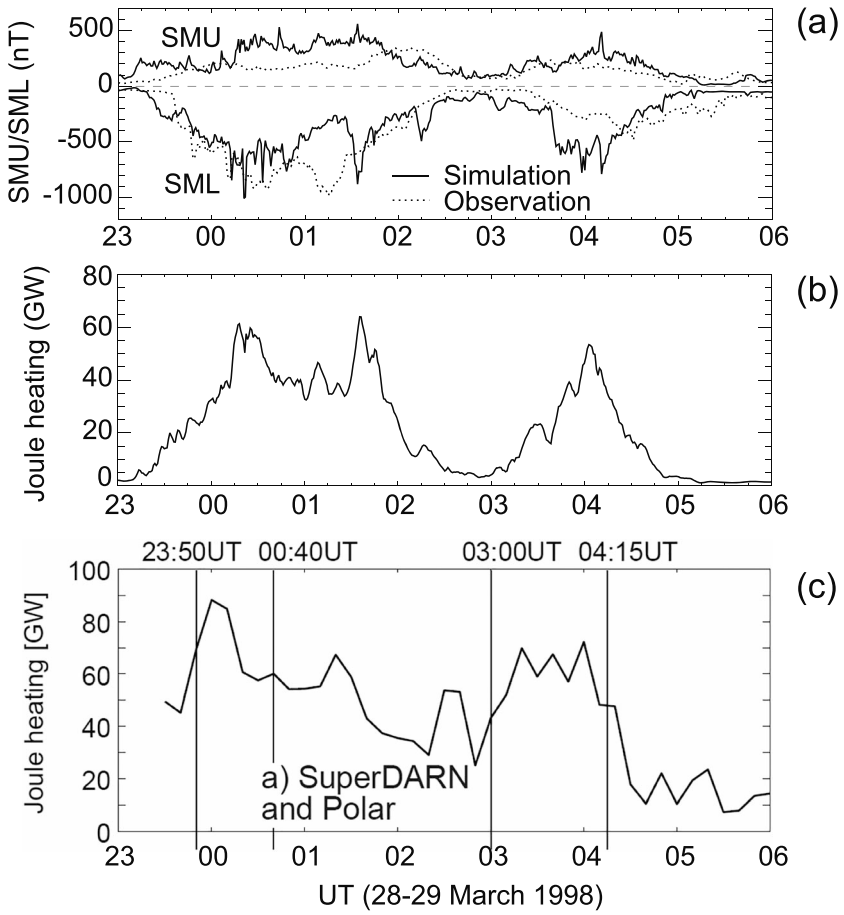

Figure A1. (a) *SMU*/*SML* indices calculated by the global magnetohydrodynamics simulation (solid) and those observed (dotted), (b) hemispheric Joule heating rate calculated by the global magnetohydrodynamics simulation, and (c) hemispheric Joule heating rate observed based on the Polar satellite and Super Dual Auroral Radar Network (SuperDARN) measurements (adapted from Palmroth et al., 2005).

simulation. In Figure A1a, the calculated SMU/SML indices are shown to agree with the observed ones. The calculated Joule heating rate in the Northern Hemisphere is given in Figure A1b, which is comparable to the one observed in the Northern Hemisphere as shown in Figure A1c (Palmroth et al., 2005). The Pedersen conductivity was calculated from the Polar satellite measurements, and the global electric field in the ionosphere was obtained by the SuperDARN radars. The agreement with the observations indicates that the global MHD simulation is capable of reproducing real substorms in terms of the auroral electrojets and the Joule heating rates

Acknowledgments
The authors thank Professor Emeritus Atsuhiro Nishida for his insightful and fruitful comments and discussion. The computer simulation was performed on the KDK computer system at the Research Institute for Sustainable Humanosphere (RISH), Kyoto University. This study was supported by JSPS KAKENHI grants 15H03732 and 15H05815. The simulation data files in the VTK format are available at the Web http://space.rish.kyoto-u.ac.jp/paper/2018-mhd-substorm/. We acknowledge the use of NASA/GSFC's Space Physics Data Facility's OMNIWeb service and OMNI data. The observed SML/SMU values are available at the Web http://supermag.jhuapl.edu/indices/.

References

Ahn, B.-H., Akasofu, S.-I., & Kamide, Y. (1983). The Joule heat production rate and the particle energy injection rate as a function of the geomagnetic indices AE and AL. *Journal of Geophysical Research*, *88*, 6275. https://doi.org/10.1029/JA088iA08p06275

Akasofu, S. I. (1981). Energy coupling between the solar wind and the magnetosphere. *Space Science Reviews*, *28*(2), 121–190. https://doi.org/10.1007/BF00218810

Akasofu, S. I. (2017). Auroral substorms: Search for processes causing the expansion phase in terms of the electric current approach. *Space Science Reviews*, *212*(1–2), 341–381. https://doi.org/10.1007/s11214-017-0363-7

Akasofu, S.-I. (1979). Interplanetary energy flux associated with magnetospheric substorms. *Planetary and Space Science*, *27*(4), 425–431. https://doi.org/10.1016/0032-0633(79)90119-3

Akasofu, S.-I. (1980). The solar wind-magnetosphere energy coupling and magnetospheric disturbances. *Planetary and Space Science*, *28*(5), 495–509. https://doi.org/10.1016/0032-0633(80)90031-8

Akasofu, S.-I. (2013). Where is the magnetic energy for the expansion phase of auroral substorms accumulated? *Journal of Geophysical Research: Space Physics*, *118*, 7219–7225. https://doi.org/10.1002/2013JA019042

Angelopoulos, V., McFadden, J. P., Larson, D., Carlson, C. W., Mende, S. B., Frey, H., et al. (2008). Tail reconnection triggering substorm onset. *Science*, *321*(5891), 931–935. https://doi.org/10.1126/science.1160495

Baker, D. N., Pulkkinen, T. I., Hesse, M., & McPherron, R. L. (1997). A quantitative assessment of energy storage and release in the Earth's magnetotail. *Journal of Geophysical Research*, *102*, 7159–7168. https://doi.org/10.1029/96JA03961

Bargatze, L. F., Baker, D. N., McPherron, R. L., & Hones, E. W. (1985). Magnetospheric impulse response for many levels of geomagnetic activity. *Journal of Geophysical Research*, *90*, 6387. https://doi.org/10.1029/JA090iA07p06387

Birn, J., & Hesse, M. (2005). Energy release and conversion by reconnection in the magnetotail. *Annales Geophysicae*, *23*(10), 3365–3373. https://doi.org/10.5194/angeo-23-3365-2005

Caan, M. N., McPherron, R. L., & Russell, C. T. (1975). Substorm and interplanetary magnetic field effects on the geomagnetic tail lobes. *Journal of Geophysical Research*, *80*, 191–194. https://doi.org/10.1029/JA080i001p00191

Cheng, C. Z., & Lui, A. T. Y. (1998). Kinetic ballooning instability for substorm onset and current disruption observed by AMPTE/CCE. *Geophysical Research Letters*, *25*, 4091–4094. https://doi.org/10.1029/1998GL900093

Cosgrove, R. B., Bahcivan, H., Chen, S., Strangeway, R. J., Ortega, J., Alhassan, M., et al. (2014). Empirical model of Poynting flux derived from FAST data and a cusp signature. *Journal of Geophysical Research: Space Physics*, *119*, 411–430. https://doi.org/10.1002/2013JA019105

Davis, T. N., & Sugiura, M. (1966). Auroral electrojet activity index AE and its universal time variations. *Journal of Geophysical Research*, *71*, 785–801. https://doi.org/10.1029/JZ071i003p00785

Ebihara, Y., & Tanaka, T. (2015a). Substorm simulation: Insight into the mechanisms of initial brightening. *Journal of Geophysical Research: Space Physics*, *120*, 7270–7288. https://doi.org/10.1002/2015JA021516

Ebihara, Y., & Tanaka, T. (2015b). Substorm simulation: Formation of westward traveling surge. *Journal of Geophysical Research: Space Physics*, *120*, 10,466–10,484. https://doi.org/10.1002/2015JA021697

Ebihara, Y., & Tanaka, T. (2017). Energy flow exciting field-aligned current at substorm expansion onset. *Journal of Geophysical Research: Space Physics*, *122*, 12,288–12,309. https://doi.org/10.1002/2017JA024294

Ebihara, Y., Tanaka, T., & Kikuchi, T. (2014). Counter equatorial electrojet and overshielding after substorm onset: Global MHD simulation study. *Journal of Geophysical Research: Space Physics*, *119*, 7281–7296. https://doi.org/10.1002/2014JA020065

Fairfield, D. H., & Cahill, L. J. (1966). Transition region magnetic field and polar magnetic disturbances. *Journal of Geophysical Research*, *71*, 155–169. https://doi.org/10.1029/JZ071i001p00155

Hesse, M. (1995). The magnetotail's role in magnetospheric dynamics: Engine or exhaust pipe. *Reviews of Geophysics*, *33*, 675–683. https://doi.org/10.1029/95RG00348

Hones, E. W. (1979). Transient phenomena in the magnetotail and their relation to substorms. *Space Science Reviews*, *23*(3), 393–410. https://doi.org/10.1007/BF00172247

Hones, E. W., Birn, J., Baker, D. N., Bame, S. J., Feldman, W. C., McComas, D. J., et al. (1984). Detailed examination of a plasmoid in the distant magnetotail with ISEE 3. *Geophysical Research Letters*, *11*, 1046–1049. https://doi.org/10.1029/GL011i010p01046

Iijima, T., & Potemra, T. A. (1976). The amplitude distribution of field-aligned currents at northern high latitudes observed by Triad. *Journal of Geophysical Research*, *81*, 2165. https://doi.org/10.1029/JA081i013p02165–2174

Kamide, Y., Craven, J. D., Frank, L. A., Ahn, B.-H., & Akasofu, S.-I. (1986). Modeling substorm current systems using conductivity distributions inferred from DE auroral images. *Journal of Geophysical Research*, *91*, 11,235. https://doi.org/10.1029/JA091iA10p11235

Kawasaki, K., Akasofu, S.-I., Yasuhara, F., & Meng, C.-I. (1971). Storm sudden commencements and polar magnetic substorms. *Journal of Geophysical Research*, *76*, 6781–6789. https://doi.org/10.1029/JA076i028p06781

King, J. H., & Papitashvili, N. E. (2005). Solar wind spatial scales in and comparisons of hourly Wind and ACE plasma and magnetic field data. *Journal of Geophysical Research*, *110*, A02104. https://doi.org/10.1029/2004JA010649

Koskinen, H. E. J., & Tanskanen, E. I. (2002). Magnetospheric energy budget and the epsilon parameter. *Journal of Geophysical Research*, *107*(A11), 1415. https://doi.org/10.1029/2002JA009283

Lui, A. T. Y., Mankofsky, A., Chang, C.-L., Papadopoulos, K., & Wu, C. S. (1990). A current disruption mechanism in the neutral sheet: A possible trigger for substorm expansions. *Geophysical Research Letters*, *17*, 745–748. https://doi.org/10.1029/GL017i006p00745

Maezawa, K. (1979). Statistical study of the dependence of geomagnetic activity on solar wind parameters. In W. P. Olson (Ed.), *Quantitative modeling of magnetospheric processes*, *Geophysical Monograph Series* (pp. 436–447). Washington, DC: American Geophysical Union.

McPherron, R. L. (1970). Growth phase of magnetospheric substorms. *Journal of Geophysical Research*, *75*, 5592–5599. https://doi.org/10.1029/JA075i028p05592

McPherron, R. L., Russell, C. T., & Aubry, M. P. (1973). Satellite studies of magnetospheric substorms on August 15, 1968: 9. Phenomenological model for substorms. *Journal of Geophysical Research*, *78*, 3131–3149. https://doi.org/10.1029/JA078i016p03131

Mozer, F. S., & Hull, A. (2001). Origin and geometry of upward parallel electric fields in the auroral acceleration region. *Journal of Geophysical Research*, *106*, 5763. https://doi.org/10.1029/2000JA900117–5778

Murayama, T. (1982). Coupling function between solar wind parameters and geomagnetic indices. *Reviews of Geophysics*, *20*, 623–629. https://doi.org/10.1029/RG020i003p00623

Murayama, T., & Hakamada, K. (1975). Effects of solar wind parameters on the development of magnetospheric substorms. *Planetary and Space Science*, *23*, 75–91. https://doi.org/10.1016/0032-0633(75)90069-0

Nagai, T., Fujimoto, M., Saito, Y., Machida, S., Terasawa, T., Nakamura, R., et al. (1998). Structure and dynamics of magnetic reconnection for substorm onsets with Geotail observations. *Journal of Geophysical Research*, *103*, 4419–4440. https://doi.org/10.1029/97JA02190

Newell, P. T., & Gjerloev, J. W. (2011). Evaluation of SuperMAG auroral electrojet indices as indicators of substorms and auroral power. *Journal of Geophysical Research*, *116*, A12211. https://doi.org/10.1029/2011JA016779

Newell, P. T., Liou, K., Gjerloev, J. W., Sotirelis, T., Wing, S., & Mitchell, E. J. (2016). Substorm probabilities are best predicted from solar wind speed. *Journal of Atmospheric and Solar-Terrestrial Physics*, *146*, 28–37. https://doi.org/10.1016/j.jastp.2016.04.019

Nishida, A. (1983). IMF control of the Earth's magnetosphere. *Space Science Reviews*, *34*(2), 185–200. https://doi.org/10.1007/BF00194626

Palmroth, M., Janhunen, P., Pulkkinen, T. I., Aksnes, A., Lu, G., Østgaard, N., et al. (2005). Assessment of ionospheric Joule heating by GUMICS-4 MHD simulation, AMIE, and satellite-based statistics: Towards a synthesis. *Annales Geophysicae*, *23*(6), 2051–2068. https://doi.org/10.5194/angeo-23-2051-2005

Palmroth, M., Pulkkinen, T. I., Janhunen, P., & Wu, C. C. (2003). Stormtime energy transfer in global MHD simulation. *Journal of Geophysical Research*, *108*(A1), 1048. https://doi.org/10.1029/2002JA009446

Papadopoulos, K., Goodrich, C., Wiltberger, M., Lopez, R., & Lyon, J. G. (1999). The physics of substorms as revealed by the ISTP. *Physics and Chemistry of the Earth, Part C: Solar, Terrestrial and Planetary Science*, *24*(1–3), 189–202. https://doi.org/10.1016/S1464-1917(98)00028-2

Perreault, P., & Akasofu, S.-I. (1978). A study of geomagnetic storms. *Geophysical Journal International*, *54*(3), 547–573. https://doi.org/10.1111/j.1365-246X.1978.tb05494.x

Richmond, A. D., Kamide, Y., Akasofu, S.-I., Alcaydé, D., Blanc, M., de la Beaujardière, O., et al. (1990). Global measures of ionospheric electrodynamic activity inferred from combined incoherent scatter radar and ground magnetometer observations. *Journal of Geophysical Research*, *95*, 1061. https://doi.org/10.1029/JA095iA02p01061

Rostoker, G., & Fälthammar, C. (1967). Relationship between changes in the interplanetary magnetic field and variations in the magnetic field at the Earth's surface. *Journal of Geophysical Research*, *72*, 5853–5863. https://doi.org/10.1029/JZ072i023p05853

Siscoe, G. L., Crooker, N. U., Erickson, G. M., Sonnerup, B. U. Ö., Siebert, K. D., Weimer, D. R., et al. (2000). Global geometry of magnetospheric currents inferred from MHD simulations. *Magnetospheric Current Systems*, *118*, 41–52. https://doi.org/10.1029/GM118p0041

Sergeev, V., Kubyshkina, M., Alexeev, I., Fazakerley, A., Owen, C., Baumjohann, W., et al. (2008). Study of near-Earth reconnection events with cluster and double Star. *Journal of Geophysical Research*, *113*, A07S36. https://doi.org/10.1029/2007JA012902

Song, Y., & Lysak, R. L. (2001). The physics in the auroral dynamo regions and auroral particle acceleration. *Physics and Chemistry of the Earth, Part C: Solar, Terrestrial & Planetary Science*, *26*(1–3), 33–42. https://doi.org/10.1016/S1464-1917(00)00087-8

Sun, W., Ahn, B. H., & Akasofu, S. I. (1985). The global joule heat production rate and the AE index. *Planetary and Space Science*, *33*(3), 279–281. https://doi.org/10.1016/0032-0633(85)90059-5

Tanaka, T. (1995). Generation mechanisms for magnetosphere-ionosphere current systems deduced from a three-dimensional MHD simulation of the solar wind-magnetosphere-ionosphere coupling processes. *Journal of Geophysical Research*, *100*, 12,057–12,074. https://doi.org/10.1029/95JA00419

Tanaka, T. (2000). Field-aligned-current systems in the numerically simulated magnetosphere. *Magnetospheric Current Systems, Geophysical Monograph Series*, *118*, 53–59.

Tanaka, T. (2007). Magnetosphere-ionosphere convection as a compound system. *Space Science Reviews*, *133*(1-4), 1–72. https://doi.org/10.1007/s11214-007-9168-4

Tanaka, T. (2015). Substorm auroral dynamics reproduced by advanced global magnetosphere–ionosphere (M-I) coupling simulation. In *Auroral Dynamics and Space Weather* (pp. 177–190). Hoboken, NJ: John Wiley & Sons, Inc. https://doi.org/10.1002/9781118978719.ch13

Tanaka, T., Ebihara, Y., Watanabe, M., Den, M., Fujita, S., Kikuchi, T., et al. (2017). Global simulation study for the time sequence of events leading to the subsorm onset. *Journal of Geophysical Research: Space Physics*, *122*, 6210–6239. https://doi.org/10.1002/2017JA024102

Tanaka, T., Watanabe, M., Den, M., Fujita, S., Ebihara, Y., Kikuchi, T., et al. (2016). Generation of field-aligned current (FAC) and convection through the formation of pressure regimes: Correction for the concept of Dungey's convection. *Journal of Geophysical Research: Space Physics*, *121*, 8695–8711. https://doi.org/10.1002/2016JA022822

Tanskanen, E., Pulkkinen, T. I., Koskinen, H. E. J., & Slavin, J. A. (2002). Substorm energy budget during low and high solar activity: 1997 and 1999 compared. *Journal of Geophysical Research*, *107*(A6), 1086. https://doi.org/10.1029/2001JA900153

Vasyliunas, V. M., Kan, J. R., Siscoe, G. L., & Akasofu, S.-I. (1982). Scaling relations governing magnetospheric energy transfer. *Planetary and Space Science*, *30*(4), 359–365. https://doi.org/10.1016/0032-0633(82)90041-1

Wang, C., Han, J. P., Li, H., Peng, Z., Richardson, J. D., & Al, W. E. T. (2014). Solar wind-magnetosphere energy coupling function fitting: Results from a global MHD. *Simulation*, *119*(8), 6199–6212. https://doi.org/10.1002/2014JA019834